MATERIALS SCIENCE

High-efficiency large-area perovskite photovoltaic modules achieved via electrochemically assembled metal-filamentary nanoelectrodes

Soonil Hong[1,2]*, Jinho Lee[2]*, Hongkyu Kang[3,4]†, Geunjin Kim[2], Seyoung Kee[2], Jong-Hoon Lee[1,2], Suhyun Jung[2], Byoungwook Park[1], Seok Kim[1], Hyungcheol Back[4], Kilho Yu[2], Kwanghee Lee[1,2,4]†

Realizing industrial-scale, large-area photovoltaic modules without any considerable performance losses compared with the performance of laboratory-scale, small-area perovskite solar cells (PSCs) has been a challenge for practical applications of PSCs. Highly sophisticated patterning processes for achieving series connections, typically fabricated using printing or laser-scribing techniques, cause unexpected efficiency drops and require complicated manufacturing processes. We successfully fabricated high-efficiency, large-area PSC modules using a new electrochemical patterning process. The intrinsic ion-conducting features of perovskites enabled us to create metal-filamentary nanoelectrodes to facilitate the monolithic serial interconnections of PSC modules. By fabricating planar-type PSC modules through low-temperature annealing and all-solution processing, we demonstrated a notably high module efficiency of 14.0% for a total area of 9.06 cm^2 with a high geometric fill factor of 94.1%.

INTRODUCTION

The unprecedented features of organic-inorganic hybrid perovskite semiconductors, which allow low-temperature crystal film growth from their precursor solutions, have greatly promoted both scientific and technological revolutions in a wide range of fields within electronics (1, 2). The advent of organolead trihalide perovskite semiconductors as light harvesters has resulted in the fastest-advancing solar technology to date, with an extremely rapid rise in power conversion efficiency (PCE) from 3.8 to 22.1% over just a few years (3–6). In addition to recent remarkable breakthroughs in addressing the instability of these devices, which has been considered the greatest challenge toward commercialization due to their intrinsic properties vulnerable to oxygen and moisture, pioneering researchers have begun fabricating large-area devices for their ultimate application (7–16). Some impressive attempts have contributed to fabricating large perovskite solar cells (PSCs) with a device size of approximately 1 cm^2 while retaining the high PCEs of small devices (~0.1 cm^2) (9–16). However, further enlarging PSCs to sizes beyond 1 cm^2 for their viable applications remain difficult, as the relatively low conductivities (that is, high sheet resistances) of existing transparent electrodes cause inevitable PCE decreases in large-area PSCs, known as "ohmic loss" (10, 17).

Currently, the only solution to this problem is introducing a module concept based on a monolithic device geometry consisting of serially connected multiple subcells with a striped pattern at a regular distance (14–16, 18–23). In this module architecture, the ohmic loss of a PSC can be alleviated, as the use of several stripe-patterned transparent electrodes with sufficiently narrow widths (approximately 10 mm) neglects the high sheet resistances of the transparent electrodes (typically ~15 ohms/square). Although a

few notable studies have demonstrated large-area PSCs using module structures, their module PCEs, calibrated using a geometric fill factor (FF; the ratio between the photoactive area and the total area), abruptly dropped compared with the PCEs of small-area PSCs (15, 16, 18–21). Such a marked performance decrease arises from an inherent weakness in ensuring contact areas for serially connected subcells, so-called aperture loss. To secure series connection regions (SCRs), in which the counter electrodes of two adjacent subcells are directly interconnected, each component layer must be patterned using delicate and complex shifting/patterning printing techniques in a layout featuring regularly spaced, cascading stacks (15, 16, 18–20). However, these processing methods produce low geometric FFs of 40 to 60%, resulting in serious PCE reduction. An alternative patterning method is to use a laser-scribing technique, which has been widely used in most existing photovoltaic technologies, to precisely pattern the subcells with small intervals and thereby maximize the geometric FFs of the modules (14, 21–26). However, the use of laser processing requires delicate installation and management and forms small particles that adhere to adjacent areas by scattering of the scribed materials, which can increase the complexity of industrial production and the failure probability in PSC quality control. Although the residue problem can be effectively prevented by optimizing laser settings and introducing proper posttreatments, the processes may increase the fabrication cost (27–31).

Here, we successfully demonstrate a new fabrication architecture for large-area PSC modules that is completely different from any conventional sophisticated patterning process. Using the intrinsic ion-conducting features of perovskite semiconductors, we devised an innovative electrochemical patterning process that achieves a perfect series connection for the modules by creating metal-filamentary nanoelectrodes inside the component layers of the SCRs. Through the consecutive patternless deposition of the component layers using low-temperature annealing and solution processing, we successfully fabricated high-performance planar-type PSC modules with no considerable concomitant ohmic or aperture losses. The resulting modules had high geometric FFs of 91.4 and 94.1% for total areas of 1.21 and 9.06 cm^2, respectively, thereby producing high module PCEs of 14.6 and 14.0%, respectively.

[1]School of Materials Science and Engineering, Gwangju Institute of Science and Technology, Gwangju 61005, Republic of Korea. [2]Heeger Center for Advanced Materials, Gwangju Institute of Science and Technology, Gwangju 61005, Republic of Korea. [3]Department of Chemistry and Centre for Plastic Electronics, Imperial College London, London SW7 2AZ, UK. [4]Research Institute for Solar and Sustainable Energies, Gwangju Institute of Science and Technology, Gwangju 61005, Republic of Korea.
*These authors contributed equally to this work.
†Corresponding author. Email: gemk@gist.ac.kr (H.K.); klee@gist.ac.kr (K.L.)

RESULTS

Module architecture

A schematic illustration of our module architecture and its corresponding energy-level diagram are shown in Fig. 1, A and B, respectively. Considering the printability of PSCs on plastic substrates, we adopted a planar device configuration fabricated without using highly crystallized and compact titanium dioxide films, which require a high sintering temperature that is difficult to apply to plastic substrates. For a photoactive layer, we used a perovskite semiconductor based on methylammonium lead triiodide ($CH_3NH_3PbI_3$) grown using one-step solvent engineering and low-temperature annealing (~100°C). To produce an inverted p-i-n structure using an indium tin oxide (ITO) bottom anode and a silver (Ag) top cathode, we introduced two charge transport layers: hole-transporting poly(triarylamine) (PTAA) and electron-transporting [6,6]-phenyl-C61-butyric acid methyl ester (PCBM). Moreover, to fabricate high-quality perovskite films with large areas, we used a polyelectrolyte, (9,9-bis(3-(N,N-dimethylamino)propyl)-2,7-fluorene)-alt-2,7-(9,9-dioctylfluorene) (PFN), as an interfacial compatibilizer; the beneficial effect of such an interfacial layer was very recently reported by our group (13). Using the PFN layer on the PTAA hole-transport layer im-proves the wettability of the hydrophilic perovskite precursor solution on hydrophobic PTAA and thereby enables the formation of large-area pinhole-free polycrystalline perovskite films without producing interfacial dipoles. Once again, we used PFN as an interfacial dipole layer on the PCBM electron transport layer (ETL) to reduce the energetic barrier between the lowest unoccupied molecular orbital level of PCBM and the work function of Ag, thus facilitating efficient electron collection at the cathode (fig. S1).

The most outstanding feature of our module structure is that all component layers are coated in a single-layer form without any striped patterning, contrasting with existing modules that include all stripe-patterned layers (32, 33). Because the ITO and Ag electrodes were only patterned in stripes with small blank offsets and slight shifts with respect to each counter electrode, we achieved very high geometric FFs of 91.4 and 94.1% for total areas of 1.21 and 9.06 cm^2, respectively, in the modules (fig. S2, A and B). Because of the small overlapping regions between the counter electrodes (referred to as SCRs) having backward diode characteristics that hamper the series connections of adjacent subcells, we anticipated that the module would not be monolithically well operated in the current state (fig. S2C). To overcome this problem,
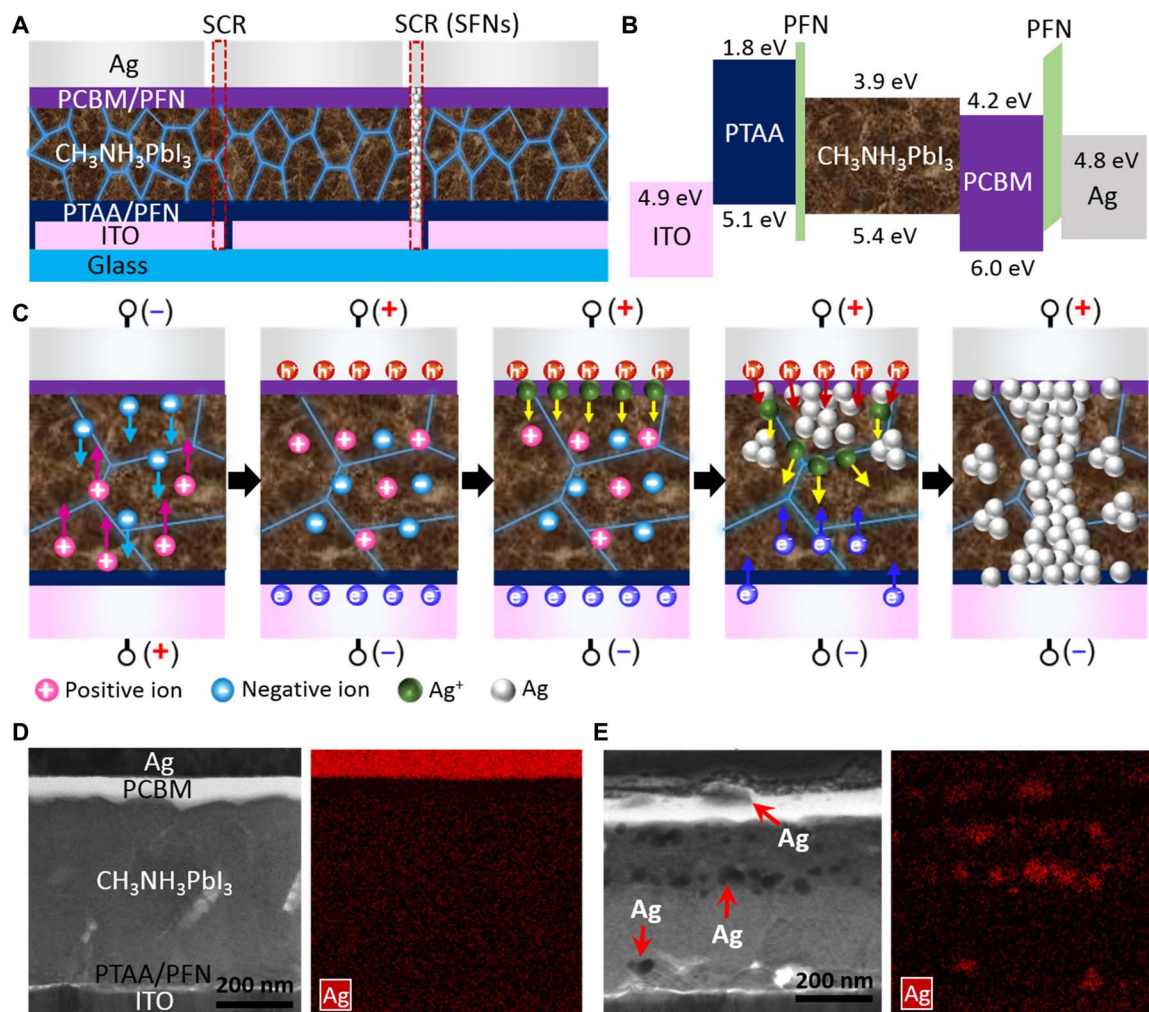
Fig. 1. Schematic illustration of the PSC module with SFNs. (**A**) Conceptual module structure comprising nonpatterned component layers before (left SCR) and after (right SCR) introducing the SFNs. (**B**) Energy-level diagram of the corresponding device. (**C**) Scheme of the SFN formation process via ion migration and electrochemical reaction. (**D** and **E**) Cross-sectional STEM images and the corresponding EDS images (D) before and (E) after the formation of the SFNs.

we invented an electrochemical patterning process that vertically forms metal-filamentary nanoelectrodes inside the component layers by applying an electric field to the SCRs, thereby leading to efficient series connections of the subcells in the PSC modules (Fig. 1C and figs. S2D and S3, A and B). On the basis of previous results indicating that creating metal filaments relies heavily on the ionic conductivity of the semiconducting materials, we expect that perovskite materials will be highly suitable for this purpose because most perovskites are well known as ionic conductors mediated by their ionic species (for example, halide or methylammonium ions) (34–36). Galvanostatic DC measurements revealed the high ionic conductivity (1.55×10^{-9} S cm^{-1}) of the perovskite film, whereas general bulk heterojunction organic blends have shown no ionic conductivity (fig. S3, C and D) (37).

Mechanism of silver filamentary nanoelectrode formation in the SCRs

On the basis of pioneering studies on metal filaments (34–36, 38, 39), we propose the following five processes for understanding the underlying mechanism of metal filament formation in the SCRs. (i) Ion redistribution: When applying a forward bias (+3 V) to the SCRs, the negatively and positively charged ions of the perovskites are redistributed toward the surfaces of the ITO and Ag electrodes, respectively. It was experimentally found that we can ensure the formation of metal filaments when applying the forward bias. This result would be presumably because evenly distributed negatively charged ions and vacancies within the whole perovskite layer by the forward bias would help to form metal

filaments. (ii) Charge accumulation: The application of a reverse bias (−3 V) induces charge accumulation of the injected charge carriers at each interface (that is, electrons at ITO and holes at Ag) between the electrode and component layer due to the rectifying characteristics of the SCRs. (iii) Metal oxidation: The accumulated holes at the Ag electrode produce Ag ions through electrochemical oxidation (Ag $\rightarrow$ Ag$^+$ + e$^-$) of the Ag electrode. (iv) Ion migration: An electric field induced by the accumulated charges at both electrode interfaces forces the generated Ag$^+$ ions to migrate to the ITO electrode via interstitial sites, and ion substitutions with redistributed positive ions are created when applying the forward bias to the SCRs. The migration direction of the Ag$^+$ ions is determined by an internal electric field across the perovskite film. (v) Ion reduction: The migrated Ag ions within the component layers are electrochemically reduced to Ag atoms (Ag$^+$ + e$^-$ $\rightarrow$ Ag) by recombining with electrons injected from the ITO anode. The reduced Ag atoms then combine to create Ag clusters near the Ag electrode and thereby form conductive silver filamentary nanoelectrodes (SFNs) within the SCRs through consecutive cycles of metal oxidation, migration, and reduction.

Analysis of SFN formation

Direct evidence of SFN formation was provided by a combined analysis involving scanning transmission electron microscopy (STEM) and energy-dispersive spectroscopy (EDS), which are powerful tools for obtaining cross-sectional images of the samples. The STEM and EDS images of the pristine SCRs show very sharp interfaces between the component layers without interlayer mixing (Fig. 1D). However,
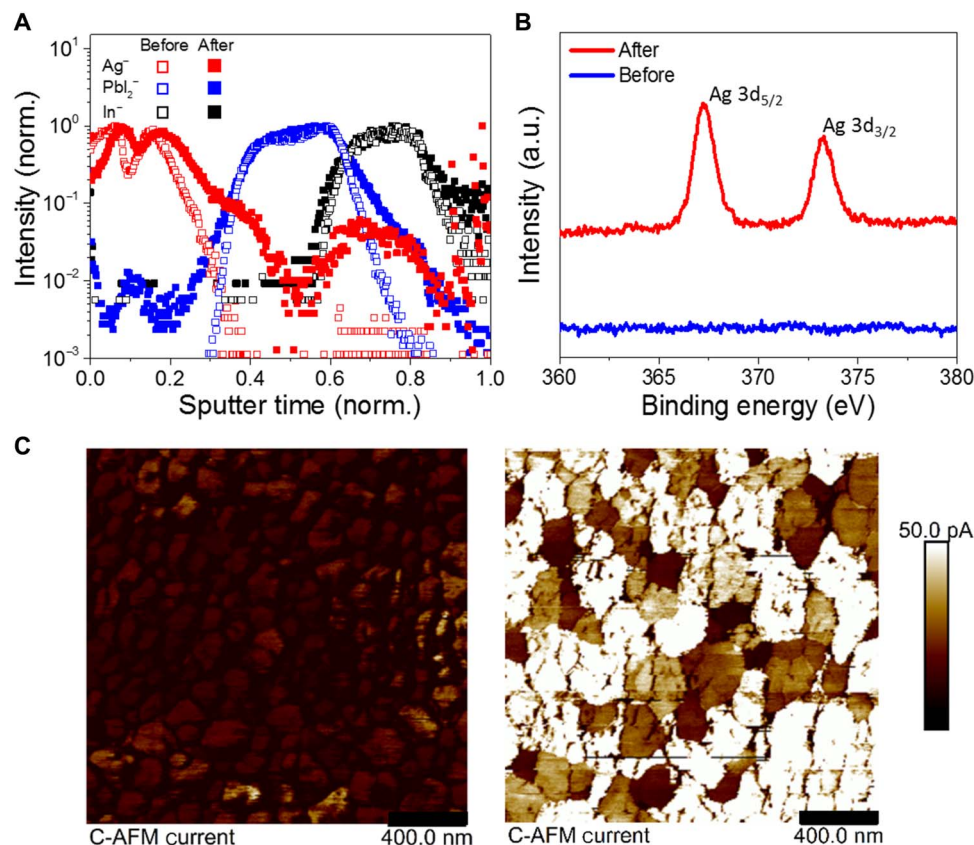

Fig. 2. Comprehensive analysis of the SFNs in the perovskite films. (A) TOF-SIMS depth profiles of all component layers before and after the formation of the SFNs. a.u., arbitrary units. (B) High-resolution XPS spectra of Ag on the perovskite films before and after the formation of the SFNs. (C) C-AFM current images of the perovskite films without (left) and with (right) SFNs.
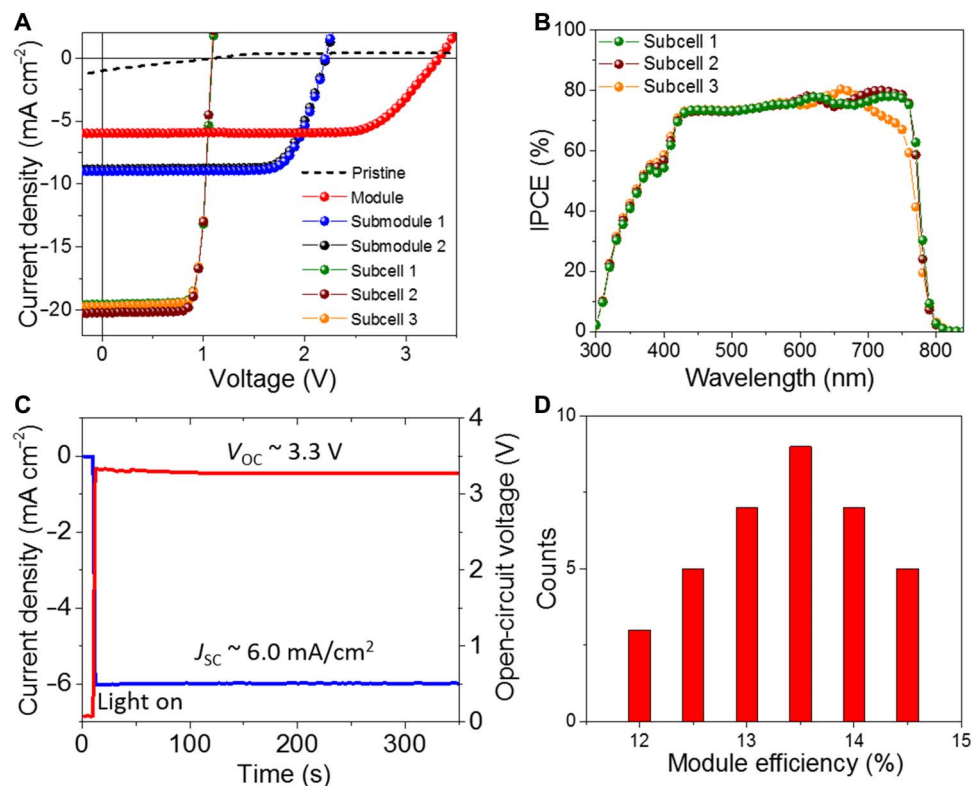
Fig. 3. Photovoltaic characterization of the PSC modules with a total area of 1.21 cm². (**A**) J-V curves of the modules with serial interconnections by the SFNs. (**B**) Incident photon-to-current efficiency (IPCE) spectra of the individual subcells. (**C**) Steady-state module J_{sc} and V_{oc} outputs over time. (**D**) Statistical efficiency distribution of the modules.

after applying a bias to the SCRs, the Ag atoms of the top electrode substantially disappeared and agglomerated to form many Ag nanoparticles diffused across the component layers (Fig. 1E). An additional vertical investigation using time-of-flight secondary ion mass spectrometry (TOF-SIMS) also confirmed that the Ag atoms in the electric field–treated sample were scattered over the entire component layers (Fig. 2A). We also examined the effects of applying an electric field to the SCRs on the surface states of the perovskite films. To directly observe the surfaces of the perovskite films, we eliminated the Ag electrode and PCBM layer from the bare and electric field–treated SCRs using a tape to detach the top electrode and chlorobenzene (CB) solvent to dissolve the PCBM layer. Then, we conducted x-ray photoelectron spectroscopy (XPS) and conductive atomic force microscopy (C-AFM) to investigate the surfaces of the samples. In the high-resolution XPS data, the bare sample exhibited no Ag binding energy peaks, whereas Ag peaks appeared in the electric field–treated sample (Fig. 2B). Moreover, the C-AFM data indicated that the surfaces of the perovskite film with the SFNs became more conductive than that of the pristine film, which was accompanied by morphological changes through the infiltration and embedding of Ag particles to form metal filaments within the component layers (Fig. 2C). Therefore, we conclude that applying an electric field to the SCRs induces SFN formation originating from the synergistic effects of the electrochemical reaction of the top Ag cathode and the high ionic conductivity of the perovskite layer.

Performance of PSC modules with SFNs

To explore the effect of SFN formation on the monolithic series connection of the modules, we fabricated PSC modules with a total area

Table 1. Performance parameters of the PSC module with a total area of 1.21 cm². APCE, PCE of the active areas of the module; MPCE, PCE of the total area of the module.

	Area (cm²)	V_{oc} (V)	I_{sc} (mA)	J_{sc} (mA cm⁻²)	FF	APCE (%)	MPCE (%)
Pristine	1.21	1.10	1.22	1.01	0.24	0.29	0.27
Module	1.21	3.32	7.21	6.00	0.74	16.0	14.6
Submodule 1	0.805	2.20	7.23	8.98	0.75	16.1	14.9
Submodule 2	0.805	2.21	7.10	8.81	0.74	15.7	14.4
Subcell 1	0.37	1.10	7.24	19.6	0.78	16.7	—
Subcell 2	0.37	1.09	7.48	20.2	0.78	17.0	—
Subcell 3	0.37	1.09	7.30	19.7	0.78	16.7	—

of 1.21 cm² and a geometric FF of 91.4% (fig. S2A). By introducing the PFN interfacial compatibilizer for the formation of high-quality large-area perovskite films, we obtained well-operating subcells with uniform and hysteresis-free device operation (Fig. 3, A and B, Table 1, and fig. S4A). As expected, the SCRs also functioned as a PSC subcell that exhibited rectifying current density–voltage (J-V) characteristics, which resulted in poor module operation, displaying a very low module PCE of 0.27% with an open-circuit voltage (V_{oc}) of 1.10 V, a short-circuit current density (J_{sc}) of 1.01 mA cm⁻², and an FF of 0.24 (Fig. 3A and

fig. S4B). However, after applying electric fields to the SCRs, the diode characteristics immediately changed to a linear J-V curve, so-called electrical breakdown, indicating that the subcells were serially interconnected by the conductive SFNs formed between the electrodes of the SCRs (fig. S4C). We confirmed that no harmful effects on the adjacent subcells arise with the application of electric fields because this process occurs only in the SCRs located between the counter electrodes of two adjacent subcells, and the subcells show excellent efficiencies without any degradation after voltage application to the SCRs (Fig. 3A). In addition, by photoluminescence (PL) mapping of the module, we confirmed the formation of multiple Ag filament pathways over the entire area of the SCRs (fig. S5). As a result, we successfully achieved a markedly enhanced module PCE of 14.6% with a V_{oc} of 3.32 V, a J_{sc} of 6.00 mA cm^{-2}, and an FF of 0.74 with highly stabilized and reproducible operation (Fig. 3, C and D).

To investigate the scalability of the modules using our new patterning method, we further increased the module size to total areas of 3.02, 6.04, and 9.06 cm^2 (Fig. 4A). We obtained a further improved geometric FF of 94.1% by stripe patterning the ITO and Ag electrodes, which had blank offsets of 100 and 150 μm, respectively, and were slightly shifted by 350 μm with respect to each counter electrode (Fig. 4B and fig. S2B). All the modules had similarly high module PCEs of more than 14%. The largest PSC module with the SFNs yielded an outstanding module PCE of 14.0% with a V_{oc} of 3.30 V, a J_{sc} of 5.88 mA cm^{-2}, and an FF of 0.72 (Fig. 4, C and D, and table S1). One high-performing module with a large area of 9.06 cm^2 was tested by the Korea Institute of Energy Research (KIER) for certification and produced a certified module PCE of 14.1%, as shown in fig. S6. In

addition, we successfully achieved high module PCEs of 15.4% in a small-sized 1.21-cm^2 module and 13.3% in a large-area 9.06-cm^2 module composed of copper (Cu) filamentary nanoelectrodes (CFNs) by replacing the expensive Ag electrodes with stable and low-cost Cu electrodes, implying that the electrochemically induced patterning process may be universally applicable for various metal electrode systems (Fig. 5, fig. S7, and table S2) (40). In addition to the electrodes, our new module concept is applicable regardless of the type of charge transport layer, including titanium oxide (TiO$_x$), zinc oxide (ZnO), and poly[N,N′-bis(4-butylphenyl)-N,N′-bis(phenyl)-benzidine] (poly-TPD; fig. S8). By using the top Cu electrodes and creating CFNs, the module stability has maintained its initial high module PCE for 18 days, indicating that metal-filamentary nanoelectrodes are stable in the SCR, as shown in Fig. 5B. Furthermore, to demonstrate the applicability of our modules using CFNs to outdoor conditions, we conducted an accelerated durability test under harsh conditions such as a relative humidity of 85% and temperature of 85°C (fig. S7B). Although module efficiency was decreased within 20 hours, the degradation was saturated and the module maintained over 70% of its initial efficiency until 185 hours. In the operational stability test, the modules exhibit gradual degradation without any abrupt reduction of efficiency and device failure (fig. S7C). Considering the fact that organometal halide perovskites are vulnerable to moisture and continuous illumination, this extent of degradation might be inevitable and attributed to the instability of the perovskite materials itself. Because the antisolvent dripping process used in this study inevitably causes marked efficiency drops for large-area PSCs due to the formation of substantial defects along a radial gradient starting from the center of the perovskite film, we expect that the module PCE and stability can be
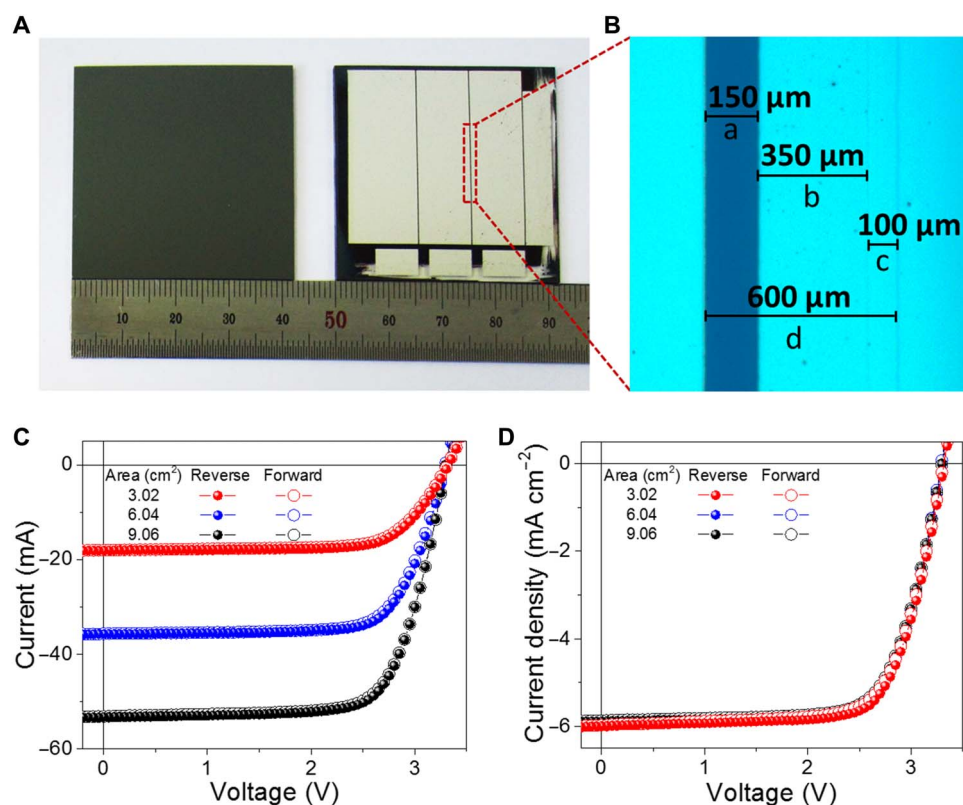
Fig. 4. Scalable fabrication of the PSC modules. (**A**) Photograph of the large-area perovskite film and completed module (total area of 9.06 cm^2). (**B**) Optical microscopy image of a module region near the SCR (a, width between the Ag electrodes; b, width of the SCR; c, width between the ITO electrodes; d, total width of the inactive area). (**C and D**) I-V (C) and J-V (D) curves of the large-area PSC modules with total areas of 3.02, 6.04, and 9.06 cm^2.
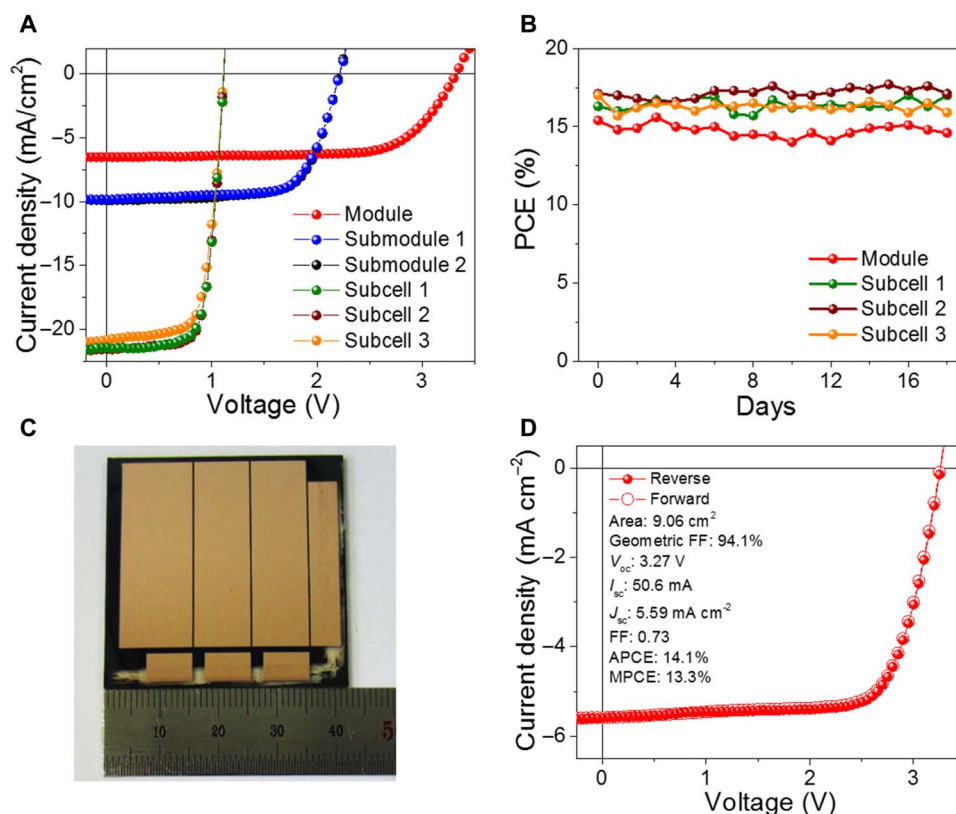
Fig. 5. PSC modules using CFNs. (**A**) *J-V* curves of the small-area 1.21-cm^2 modules using CFNs. (**B**) PCEs as a function of N$_2$ storage time without additional encapsulation. (**C**) Photograph and (**D**) corresponding *J-V* curves of the large-area 9.06-cm^2 PSC module using CFNs.

further improved by combining an innovative solution processing method for the uniform and pinhole-free fabrication of large-area perovskite films with our new electrochemical patterning concept.

DISCUSSION

In conclusion, we devised an innovative patterning method for the fabrication of planar-type and large-area PSC modules without introducing any conventional patterning process. We demonstrated the formation of metal-filamentary nanoelectrodes by the synergistic effect of the electrochemical reaction of the metal (Ag or Cu) electrode and the ion-conducting properties of the perovskite, enabling excellent serial interconnections of the counter electrodes of the subcells in the modules. As a result, we successfully achieved monolithic module operation with high module PCEs of 14.0% for a total area of 9.06 cm^2, which were properly calibrated by their high geometric FFs. On the basis of our approach, we recommend the application of this electrochemically induced metal-filament concept in various perovskite-related studies. These findings represent technological progress from small-area devices to large-area modules for practical applications of PSC systems.

MATERIALS AND METHODS

Material preparation

A 1.5 M CH$_3$NH$_3$PbI$_3$ solution was prepared by dissolving PbI$_2$ (99.9985%; Alfa Aesar) and CH$_3$NH$_3$I$_3$ (Dyesol) powder (molar ratio, 1.5:1.45) in a mixed solvent of anhydrous *N,N*-dimethylformamide/dimethylsulfoxide (volume ratio, 87:13; Sigma-Aldrich). PFN

(1-Material) was dissolved in anhydrous methanol (Sigma-Aldrich) at concentrations of 0.1 and 0.25 mg/ml. The TiO$_x$ precursor solution was prepared following the previously reported synthetic route (8). The ZnO nanoparticle (2.5% in mixed alcohol; Nano Clean Tech) solution was diluted in isopropanol to 1%. The poly-TPD (1-Material) solution was prepared by dissolving in CB at a concentration of 2 mg/ml. PTAA and PCBM solutions were prepared by dissolving PTAA (1-Material) and PCBM (Nano-C) in toluene (Sigma-Aldrich) at a concentration of 2 mg/ml and in CB (Sigma-Aldrich) at a concentration of 40 mg/ml.

Device fabrication

To fabricate the PSCs and PSC modules, all component materials were spin-coated in a N$_2$-filled glove box. The patterned glass/ITO substrates were cleaned with detergent and then sequentially ultrasonicated in deionized water, acetone, and isopropyl alcohol. The PTAA solution was spin-coated onto a glass/ITO substrate at 3000 rpm for 30 s and then dried at 40°C for 5 min. In case of the poly-TPD layer, the solution was spin-coated onto a glass/ITO substrate at 3000 rpm for 30 s and then dried at 150°C for 10 min to obtain cross-linking reaction. For the interfacial compatibilizer, the PFN solution (0.1 mg/ml) was spin-coated onto the ITO/PTAA substrate at 3000 rpm for 30 s. The perovskite precursor solution was spin-coated at 3000 rpm for 80 s. During the spin-coating (after 12 s), the perovskite layer was treated using a diethyl ether dropping process (the dropping volume was carefully controlled from 1 to 3 ml according to the device size) and then annealed at 60°C for 1 min and 100°C for 10 min. To serve as an ETL, the PCBM solution was spin-coated at 1600 rpm for 40 s and then annealed at 80°C for 3 min. To serve as an interfacial layer, the PFN

solution (0.25 mg/ml) was spin-coated at 1600 rpm for 30 s, and the TiO_x precursor and ZnO nanoparticle solutions were spin-coated at 3000 rpm for 20 s on top of PCBM. The fabrication of the PSC was completed by evaporating a Ag electrode under high-vacuum conditions (10^{-6} torr). To fabricate the PSC modules, Ag was deposited to obtain the SCRs through a stripe-patterned mask. To create the SFNs in the SCRs of the modules, forward (+3 V for 5 s) and reverse (−3 V for 10 s) biases were sequentially applied to the SCRs to connect the subcells. Then, reverse and forward sweeps (usually two times) were performed to ensure the series connection. After serially connecting subcell 1 and subcell 2, the same process was performed to serially connect subcell 2 and subcell 3.

Characterization

The current-voltage (I-V) characteristics of the devices were measured using an Iviumsoft apparatus with simulated air mass (AM) 1.5 illumination (100 mW cm^{-2}) via a solar simulator (Abet Technologies Sun 3000) under normal atmospheric conditions. The module exhibiting the best PCE was encapsulated using glass and ultraviolet curing adhesive and then sent to the KIER for certification. The details of the measurement conditions for the certification are described in fig. S8. IPCE spectra were measured using a Solar Cell Spectral Response/QE/IPCE measuring system (PV Measurements Inc.) with a chopping frequency of 100 Hz. Cross-sectional image samples of the PSC modules were prepared using a dual-beam focused ion beam (Helios NanoLab). The TEM, STEM, and EDS images were obtained using an FEI Tecnai G^2 F30 S-Twin microscope operated at 200 kV. The XPS measurements were performed using a K-Alpha$^+$ XPS spectrometer (Thermo Fisher Scientific) with monochromatized Al-Kα x-ray photons (spot size, 400 µm; energy resolution, 0.5 eV full width at half maximum). Topography and current images were obtained using a MultiMode AFM Nanoscope V controller (Bruker). Scanning electron microscopy (SEM) images were obtained using an S-4700 SEM instrument (Hitachi). PL mapping was conducted using an RPM 2000 spectrometer (Accent Optical Technologies). The stability test under a relative humidity of 85% and temperature of 85°C was performed using a humidity and temperature controller (Labmate). The photostability test for the PSC module was conducted in a glove box filled with N_2 under continuous AM 1.5 global illumination without any encapsulations.

Galvanostatic DC measurements

The galvanostatic DC measurements were conducted using a PGSTAT30 Autolab system (Eco Chemie). The galvanostatic characteristics were obtained with a time interval of 0.1 s and a constant current of 100 nA. The ionic conductivity was extracted from the mixed conductivity by subtracting the electronic conductivity from the total conductivity

$$\sigma_{total} = \sigma_{ion} - \sigma_e$$

In addition, each conductivity was derived by the following equation

$$\sigma(\Omega \cdot cm)^{-1} = \frac{1}{R}\frac{l}{A}$$

where l is the thickness of the mixed conductor film, A is the effective electrode area, and R is the resistance.

SUPPLEMENTARY MATERIALS

Supplementary material for this article is available at http://advances.sciencemag.org/cgi/content/full/4/8/eaat3604/DC1

Fig. S1. Performance of the 1-cm^2 PSCs.
Fig. S2. Geometrical FFs and equivalent circuits of the PSC modules.
Fig. S3. Scheme of ion redistribution when applying forward bias and galvanostatic DC measurements.
Fig. S4. The J-V curves of the PSC module and SCR.
Fig. S5. Photograph and PL mapping images of the PSC module.
Fig. S6. Certificated I-V curve and performance parameters of the PSC module.
Fig. S7. Stability test for the PSC modules using CFNs.
Fig. S8. PSC modules with various charge transport layers.
Table S1. Performance parameters of the large-area PSC modules with different total areas.
Table S2. Performance parameters of the 1.21-cm^2 PSC module using CFNs.

REFERENCES AND NOTES

1. S. D. Stranks, H. J. Snaith, Metal-halide perovskites for photovoltaic and light-emitting devices. *Nat. Nanotechnol.* **10**, 391–402 (2015).
2. N.-G. Park, M. Grätzel, T. Miyasaka, K. Zhu, K. Emery, Towards stable and commercially available perovskite solar cells. *Nat. Energy* **1**, 16152 (2016).
3. A. Kojima, K. Teshima, Y. Shirai, T. Miyasaka, Organometal halide perovskites as visible-light sensitizers for photovoltaic cells. *J. Am. Chem. Soc.* **131**, 6050–6051 (2009).
4. M. M. Lee, J. Teuscher, T. Miyasaka, T. N. Murakami, H. J. Snaith, Efficient hybrid solar cells based on meso-superstructured organometal halide perovskites. *Science* **338**, 643–649 (2012).
5. H.-S. Kim, C.-R. Lee, J.-H. Im, K.-B. Lee, T. Moehl, A. Marchioro, S.-J. Moon, R. Humphry-Baker, J.-H. Yum, J. E. Moser, M. Grätzel, N.-G. Park, Lead iodide perovskite sensitized all-solid-state submicron thin film mesoscopic solar cell with efficiency exceeding 9%. *Sci. Rep.* **2**, 591 (2012).
6. W. S. Yang, B.-W. Park, E. H. Jung, N. J. Jeon, Y. C. Kim, D. U. Lee, S. S. Shin, J. Seo, E. K. Kim, J. H. Noh, S. I. Seok, Iodide management in formamidinium-lead-halide–based perovskite layers for efficient solar cells. *Science* **356**, 1376–1379 (2017).
7. H. Tan, A. Jain, O. Voznyy, X. Lan, F. P. G. Arquer, J. Z. Fan, R. Quintero-Bermudez, M. Yuan, B. Zhang, Y. Zhao, F. Fan, P. Li, L. N. Quan, Y. Zhao, Z.-H. Lu, Z. Yang, S. Hoogland, E. H. Sargent, Efficient and stable solution-processed planar perovskite solar cells via contact passivation. *Science* **355**, 722–726 (2017).
8. H. Back, G. Kim, J. Kim, J. Kong, T. K. Kim, H. Kang, H. Kim, J. Lee, S. Lee, K. Lee, Achieving long-term stable perovskite solar cells via ion neutralization. *Energy Environ. Sci.* **9**, 1258–1263 (2016).
9. W. Chen, Y. Wu, Y. Yue, J. Liu, W. Zhang, X. Yang, H. Chen, E. Bi, I. Ashraful, M. Grätzel, L. Han, Efficient and stable large-area perovskite solar cells with inorganic charge extraction layers. *Science* **350**, 944–948 (2015).
10. M. Yang, Y. Zhou, Y. Zeng, C.-S. Jiang, N. P. Padture, K. Zhu, Square-centimeter solution-processed planar $CH_3NH_3PbI_3$ perovskite solar cells with efficiency exceeding 15%. *Adv. Mater.* **27**, 6363–6370 (2015).
11. Y. Wu, X. Yang, W. Chen, Y. Yue, M. Cai, F. Xie, E. Bi, A. Islam, L. Han Wu, Perovskite solar cells with 18.21% efficiency and area over 1 cm^2 fabricated by heterojunction engineering. *Nat. Energy* **1**, 16148 (2016).
12. X. Li, D. Bi, C. Yi, J.-D. Décoppet, J. Luo, S. M. Zakeeruddin, A. Hagfeldt, M. Grätzel, A vacuum flash–assisted solution process for high-efficiency large-area perovskite solar cells. *Science* **353**, 58–62 (2016).
13. J. Lee, H. Kang, G. Kim, H. Back, J. Kim, S. Hong, B. Park, E. Lee, K. Lee, Achieving large-area planar perovskite solar cells by introducing an interfacial compatibilizer. *Adv. Mater.* **29**, 1606363 (2017).
14. M. Yang, Z. Li, M. O. Reese, O. G. Reid, D. H. Kim, S. Siol, T. R. Klein, Y. Yan, J. J. Berry, M. F. A. M. van Hest, K. Zhu, Perovskite ink with wide processing window for scalable high-efficiency solar cells. *Nat. Energy* **2**, 17038 (2017).
15. H.-C. Liao, P. Guo, C.-P. Hsu, M. Lin, B. Wang, L. Zeng, W. Huang, C. M. M. Soe, W.-F. Su, M. J. Bedzyk, M. R. Wasielewski, A. Facchetti, R. P. H. Chang, M. G. Kanatzidis, T. J. Marks, Enhanced efficiency of hot-cast large-area planar perovskite solar cells/modules having controlled chloride incorporation. *Adv. Energy Mater.* **7**, 1601660 (2017).
16. C.-H. Chiang, M. K. Nazeeruddin, M. Grätzel, C.-G. Wu, The synergistic effect of H_2O and DMF towards stable and 20% efficiency inverted perovskite solar cells. *Energy Environ. Sci.* **10**, 808–817 (2017).
17. W.-I. Jeong, J. Lee, S.-Y. Park, J.-W. Kang, J.-J. Kim, Reduction of collection efficiency of charge carriers with increasing cell size in polymer bulk heterojunction solar cells. *Adv. Funct. Mater.* **21**, 343–347 (2011).
18. J. H. Heo, H. J. Han, D. Kim, T. K. Ahn, S. H. Im, Hysteresis-less inverted $CH_3NH_3PbI_3$ planar perovskite hybrid solar cells with 18.1% power conversion efficiency. *Energy Environ. Sci.* **8**, 1602–1608 (2015).

19. J. H. Heo, M. H. Lee, M. H. Jang, S. H. Im, Highly efficient $CH_3NH_3PbI_{3-x}Cl_x$ mixed halide perovskite solar cells prepared by re-dissolution and crystal grain growth via spray coating. *J. Mater. Chem. A* **4**, 17636–17642 (2016).

20. J.-S. Yeo, C.-H. Lee, D. Jang, S. Lee, S. M. Jo, H.-I. Joh, D.-Y. Kim, Reduced graphene oxide-assisted crystallization of perovskite via solution process for efficient and stable planar solar cells with module-scales. *Nano Energy* **30**, 667–676 (2016).

21. S. Razza, F. D. Giacomo, F. Matteocci, L. Cinà, A. L. Palma, S. Casaluci, P. Cameron, A. D'Epifanio, S. Licoccia, A. Reale, T. M. Brown, A. D. Carlo, Perovskite solar cells and large area modules (100 cm²) based on an air flow-assisted PbI₂ blade coating deposition process. *J. Power Sources* **277**, 286–291 (2015).

22. W. Qiu, T. Merckx, M. Jaysankar, C. Masse de la Huerta, L. Rakocevic, W. Zhang, U. W. Paetzold, R. Gehlhaar, L. Froyen, J. Poortmans, D. Cheyns, H. J. Snaith, P. Heremans, Pinhole-free perovskite films for efficient solar modules. *Energy Environ. Sci.* **9**, 484–489 (2016).

23. H. Chen, F. Ye, W. Tang, J. He, M. Yin, Y. Wang, F. Xie, E. Bi, X. Yang, M. Grätzel, L. Han, A solvent- and vacuum-free route to large-area perovskite films for efficient solar modules. *Nature* **550**, 92–95 (2017).

24. L. Lucera, P. Kubis, F. W. Fecher, C. Bronnbauer, M. Turbiez, K. Forberich, T. Ameri, H.-J. Egelhaaf, C. J. Brabec, Guidelines for closing the efficiency gap between hero solar cells and roll-to-roll printed modules. *Energy Technol.* **3**, 373–384 (2015).

25. G. D. Spyropoulos, C. O. R. Quiroz, M. Salvador, Y. Hou, N. Gasparini, P. Schweizer, J. Adams, P. Kubis, N. Li, E. Spiecker, T. Ameri, H.-J. Egelhaaf, C. J. Brabec, Organic and perovskite solar modules innovated by adhesive top electrode and depth-resolved laser patterning. *Energy Environ. Sci.* **9**, 2302–2313 (2016).

26. M. L. Petrus, J. Schlipf, C. Li, T. P. Gujar, N. Giesbrecht, P. Müller-Buschbaum, M. Thelakkat, T. Bein, S. Hüttner, P. Docampo, Capturing the sun: A review of the challenges and perspectives of perovskite solar cells. *Adv. Energy Mater.* **7**, 1700264 (2017).

27. S. Nakano, T. Matsuoka, S. Kiyama, H. Kawata, N. Nakamura, Y. Nakashima, S. Tsuda, H. Nishiwaki, M. Ohnishi, I. Nagaoka, Laser patterning method for integrated type a-Si solar cell submodules. *Jpn. J. Appl. Phys.* **25**, 1936–1943 (1986).

28. S. Haas, A. Gordijn, H. Stiebig, High speed laser processing for monolithical series connection of silicon thin-film modules. *Prog. Photovolt. Res. Appl.* **16**, 195–203 (2008).

29. S. Röttinger, B. Schwarz, S. Schäfer, R. Gauch, B. Zimmermann, U. Würfel, Laser patterning of vacuum processed small molecular weight organic photovoltaics. *Sol. Energy Mater. Sol. Cells* **154**, 35–41 (2016).

30. Z. Song, C. L. McElvany, A. B. Phillips, I. Celik, P. W. Krantz, S. C. Watthage , G. K. Liyanage, D. Apul, M. J. Heben, A technoeconomic analysis of perovskite solar module manufacturing with low-cost materials and techniques. *Energy Environ. Sci.* **10**, 1297–1305 (2017).

31. M. Graetzel, R. A. J. Janssen, D. B. Mitzi, E. H. Sargent, Materials interface engineering for solution-processed photovoltaics. *Nature* **488**, 304–312 (2012).

32. F. C. Krebs, T. Tromholt, M. Jorgensen, Upscaling of polymer solar cell fabrication using full roll-to-roll processing. *Nanoscale* **2**, 873 (2010).

33. S. Hong, H. Kang, G. Kim, S. Lee, S. Kim, J.-H. Lee, J. Lee, M. Yi, J. Kim, H. Back, J.-R. Kim, K. Lee, A series connection architecture for large-area organic photovoltaic modules with a 7.5% module efficiency. *Nat. Commun.* **7**, 10279 (2016).

34. Y. Yang, P. Gao, L. Li, X. Pan, S. Tappertzhofen, S. Choi, R. Waser, I. Valov, W. D. Lu, Electrochemical dynamics of nanoscale metallic inclusions in dielectrics. *Nat. Commun.* **5**, 4232 (2014).

35. J.-Y. Chen, C.-W. Huang, C.-H. Chiu, Y.-T. Huang, W.-W. Wu, Switching kinetic of VCM-based memristor: Evolution and positioning of nanofilament. *Adv. Mater.* **27**, 5028–5033 (2015).

36. N. R. Hosseini, J.-S. Lee, Resistive switching memory based on bioinspired natural solid polymer electrolytes. *ACS Nano* **9**, 419–426 (2015).

37. Y.-C. Zhao, W.-K. Zhou, X. Zhou, K.-H. Liu, D.-P. Yu, Q. Zhao, Quantification of light-enhanced ionic transport in lead iodide perovskite thin films and its solar cell applications. *Light Sci. Appl.* **6**, e16243 (2017).

38. C. Eames, J. M. Frost, P. R.F. Barnes, B. C. O'Regan, A. Walsh, M. S. Islam, Ionic transport in hybrid lead iodide perovskite solar cells. *Nat. Commun.* **6**, 7497 (2015).

39. Y. Yuan, J. Huang, Ion migration in organometal trihalide perovskite and its impact on photovoltaic efficiency and stability. *Acc. Chem. Res.* **49**, 286–293 (2016).

40. J. Zhao, X. Zheng, Y. Deng, T. Li, Y. Shao, A. Gruverman, J. Shield, J. Huang, Is Cu a stable electrode material in hybrid perovskite solar cells for a 30-year lifetime? *Energy Environ. Sci.* **9**, 3650–3656 (2016).

Citation: S. Hong, J. Lee, H. Kang, G. Kim, S. Kee, J.-H. Lee, S. Jung, B. Park, S. Kim, H. Back, K. Yu, K. Lee, High-efficiency large-area perovskite photovoltaic modules achieved via electrochemically assembled metal-filamentary nanoelectrodes. *Sci. Adv.* **4**, eaat3604 (2018).